

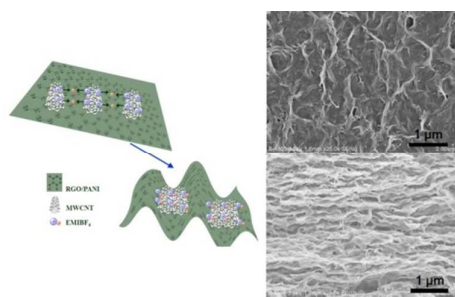


**Ionic Liquid Directed Assembly of Wrinkled and Porous
Composite Electrode for High-Power Flexible
Supercapacitors**

Journal:	<i>RSC Advances</i>
Manuscript ID:	RA-ART-09-2014-011188.R1
Article Type:	Paper
Date Submitted by the Author:	15-Nov-2014
Complete List of Authors:	Kong, Lirong; Suzhou Institute of Nano-Tech and Nano-Bionics, Chinese Academy of Sciences, i-Lab Chen, Wei; Suzhou Institute of Nano-Tech and Nano-Bionics, Chinese Academy of Sciences, i-Lab

Table of contents entry:

By using carbon nanotube/ionic liquid as surfactant-like agent, flexible reduced graphene oxide/polyaniline composite electrode membranes with wrinkled and porous structure were fabricated for high performance supercapacitors.



ARTICLE

Ionic Liquid Directed Assembly of Wrinkled and Porous Composite Electrode for High-Power Flexible Supercapacitors

Cite this: DOI: 10.1039/x0xx00000x

Received 00th January 2012,

Accepted 00th January 2012

DOI: 10.1039/x0xx00000x

www.rsc.org/

Lirong Kong and Wei. Chen*

To meet the pressing demands for portable and flexible electronic devices in contemporary society, it is strongly required to develop next-generation flexible and sustainable supercapacitors with high capacitance, high energy and power densities. Here, by using carbon nanotube/ionic liquid as surfactant-like agent, a flexible all-solid-state supercapacitor device with three-dimensional (3D) reduced graphene oxide/polyaniline composite electrode membranes was fabricated. The fabrication process relies on the surfactant like structure of ILs which contains both ionic and aromatic groups. As the aromatic groups have a tendency to make strong π - π interaction with aromatic carbons, the self-assembly process of ILs also brings the organization of the attached carbon composite materials into wrinkled and porous nanostructure. The obtained pliable supercapacitor can deliver a high specific capacitance of 154.12 F/g, a high power density of 17.21 kW/kg and a stable cycling durability with 86.3% capacitance retention after 1000 charge-discharge cycles. The high performance of the as-prepared electrode film was ascribed to its unique nanostructure composed of micro and mesopores. The ionic liquid directed assembly method developed here also provided a new idea for structural controlled preparation of graphitic carbon nanomaterials.

INTRODUCTION

Nowadays, the popularization of commercialized pocket electronic devices, such as wearable or foldable electronics, electronic papers and mobile electronic devices, make the development of inexpensive, flexible and light weight energy storage devices a priority.¹⁻³ Among these devices, electrochemical capacitors (ECs, also called supercapacitors) have attracted increased attention due to their high capacitance, high power density, long-cycle life and fast charge/discharge rate.⁴⁻⁷ However, the low energy density of ECs may limit their wide application in commercial devices.⁸ Compared to electric double-layer capacitive electrode materials, pseudocapacitive electrode materials, such as transitional metal oxides and conducting polymers, usually exhibit higher capacitance and energy densities and thus may provide an opportunity to satisfy the needs for high-performance supercapacitors.⁹⁻¹⁰

Among pseudocapacitive materials, polyaniline (PANI) is one of the most promising conducting polymers because of its high environmental stability, high specific capacitance, low cost and synthetic easiness.¹¹⁻¹² However, chemically synthesized PANI

always suffers from low conductivity and rapid structural degradation during successive charge/discharge process due to its swelling and shrinkage, which result in their poor charge storage capability and cyclic performance.¹³⁻¹⁴ Combing PANI with conductive nanocarbon materials, such as graphene and carbon nanotubes, provides a promising way to enhance its electrochemical performance and cyclic stability.¹⁵⁻¹⁶ It is interesting that the PANI/nanocarbon composite materials usually possess higher specific capacitance, energy density and power density than those of pure PANI and nanocarbon. This could be ascribed to the unique doping process of PANI¹⁷ and charge transfer with conductive carbon materials¹⁸. Moreover, after being composed with nanocarbon materials, PANI usually exists as nanoparticles or nanocoatings. Owing to the structural confinement effect, its structural swelling and shrinkage as well as the degradation extent could be well restricted when compared with bulk PANI.

Among various conductive nanocarbon materials, graphene is a good candidate for electrode materials because of its large surface area (high up to 2600-2700 m²/g), fascinating electronic and mechanical properties. Recently, a great many research

groups focused on the incorporation of graphene into PANI to improve its rate capability, charge/discharge stability and specific capacitance.¹⁹⁻²² For example, Tour's group grew PANI nanorods on graphene nanoribbons and the obtained product exhibits a high specific capacitance of 340 F/g at a current density of 0.25 A/g also in 1 mol L⁻¹ H₂SO₄ aqueous solution.²⁰ Sawangphruk et al. reported the fabrication of an all-solid-state supercapacitor with Ag nanoparticle-PANI-graphene/carbon nanofiber paper electrode and a PVA-gelled NaNO₃ electrolyte layer which exhibited 142 F/g under 1.5 A/g.²²

However, as the graphene layers are apt to restack together due to the strong π - π interaction, even when it was coated with PANI layer, the migration of electrolyte ions into the graphene/PANI layers was hindered, especially at high charge-discharge rates.²³ Thus the energy density as well as the power density was relatively low for the above graphene/PANI composite electrode based ECs. In order to overcome the restacking problem, scientists have tried to prepare three-dimensional (3D) graphene/PANI electrode films mainly by the template method or self-assembly hydrogel method.²⁴ The diameter of pores in the films prepared by the above two methods were usually too large (hundreds of nanometers to several micrometers) for ion insertion and may cause a decrease in mechanical properties of the electrode films. According to Vix-Guterl et al., adapting the pore size to that of the electrolyte ions is crucial for optimizing the performance of supercapacitors and in most circumstances, a well-balanced microporosity is preferable since the micropores determine the high surface area on which ions are adsorbed and the mesopores are essential for ions transportation.²⁵⁻²⁶ Hence in this work, we proposed a self-assembly method to prepare 3D graphene/PANI composite film by using multiwalled carbon nanotubes (MWCNTs)/ionic liquid (IL) as the surfactant-like agent. According to Ozkan et al., carbon nanotubes could be well dispersed in GO solution through π - π interaction, and this was also applicable for the RGO/PANI/MWCNTs/IL system.²⁷ Moreover, in our experiment, the fabrication process for the 3D porous structure mainly relies on the surfactant like structure of ILs which contains both ionic and aromatic groups.²⁸ As the aromatic groups have a tendency to make strong π - π interaction with aromatic carbons, the self-assembly process of ILs also brings the organization of the attached carbon composite materials into wrinkled and porous nanostructure. By using this method, the pore structure in the composite electrode film could be well controlled as only micropores and mesopores, without macropores. The obtained 3D electrode film based flexible capacitor exhibits high capacitance, energy density and power density than those ones without 3D porous structure.

EXPERIMENTAL SECTION

Materials

Natural graphite flake (325 meshes, 99.8%, ABCR GmbH & Co. KG) was obtained from Sigma Aldrich. Phosphorous oxide (purity 98%) and potassium peroxydisulfate (purity 97%) was obtained from Alfa Aesar. MWCNTs (8-15 nm in diameter) used in this work were purchased from Shenzhen Nanotech. Port. Co., Ltd. (China). Poly (vinylidene fluoride-co-hexafluoropropylene) (PVDF-HFP, Mw=400,000) was obtained from Sigma-aldrich. All other chemicals were obtained from Sinopharm Chemical Reagent Co., Ltd and deionized water was purified through Ultrapure Milli-Q system. Aniline monomer was distilled under reduced pressure and stored below 0 °C before use. Other reagents were analytical grade and used without further purification, including ammonium persulfate (APS), NH₃·H₂O, N₂H₄·H₂O, sulfosalicylic acid (SSA), N-methylpyrrolidone (NMP), N,N-dimethylformamide (DMF), propylene carbonate (PC) and 1-ethyl-3-methylimidazolium tetrafluoroborate (EMIBF₄).

Preparation of Graphene Oxide (GO)/PANI Composite

0.24 g Aniline was added to 150 mL GO solution (1.6 mg/mL) and stirred for 30 min to make Aniline completely dissolved. 0.591g APS was dissolved in 30 mL distilled water. After cooling the above two solutions at 0-5 °C for 30 min, they were quickly mixed together and then reacted at 0-5 °C for 15 h. The obtained product was filtered, washed several times by ethanol and water, and then dispersed in distilled water at a concentration of 1-2 mg/mL.

Preparation of Reduced Graphene Oxide (RGO)/PANI/MWCNT/IL Electrode Membranes

MWCNTs were added into the above dispersion and the weight ratio of MWCNTs to GO/PANI was 1:9. The mixture was horn sonicated (200 W) for accumulated 15 min in a program of 2s on and 3s off in ice water bath and then reduced to RGO/PANI/MWCNT with N₂H₄·H₂O following the method of obtaining RGO.²⁹ The reduced product was filtered, washed by water for three times and then doped in SSA aqueous solution (0.1 mol/L) for more than 6h. The doped RGO/PANI/MWCNT composites was filtered, washed by ethanol and then dispersed in NMP at a concentration of 5 mg/mL. EMIBF₄ with equivalent weight to RGO/PANI/MWCNT was added to the above dispersion and then under gone 200 W horn sonication for accumulated 15 min. By casting 3 mL of the RGO/PANI/MWCNT/IL dispersion on a 7.5×2.5 cm² area glass substrate and evaporates the solvent on a heating plate at 80 °C for 4 h, the hybrid electrode film (15 mg) was obtained.

Electrochemical Measurement

The electrolyte membrane was prepared by casting 3 mL DMF solution containing 75 mg PVDF-HFP, 150 mg EMIBF₄ and 187.5 mg PC on a 7.5×2.5 cm² area glass substrate and evaporates the solvent at 80 °C. Two pieces of same electrode membranes were laminated on a electrolyte membrane and hot-pressed under 150 °C overnight, obtaining uniform black all-solid-state supercapacitors. A capacitor strip of 10 mm×3 mm was cut from the whole piece and clamped between two gold coated copper electrodes. The specific capacitance of the supercapacitor cell was calculated from the

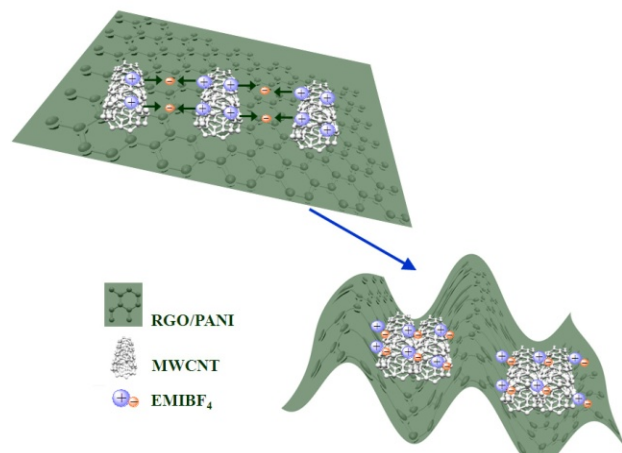
equation of $C_{cell} = It/m\Delta V$ 错误!未定义书签。 , where I is the discharge current, Δt is the discharge time, m is the total mass of active materials in two electrodes, and ΔV is the voltage drop upon discharge (excluding IR drop). In symmetric supercapacitors, the specific capacitance (C) of the electrodes was calculated according to $C = 4C_{cell}$. The energy density (E) and power density (P) of a supercapacitor cell in the Ragone plots were calculated following the equations of $E = 1/2C_{cell}\Delta V^2$ and $P = E/\Delta t$, respectively.³⁰⁻³²

Equipments

Exfoliation of graphite oxide to GO was achieved by sonication of its dispersion using a Digital Sonifier (KQ3200DA, 150 W, 100%). Sonication assisted dispersing of GO/PANI/MWCNT was achieved by using a Fisher Scientific model 500 digital sonic dismembrator equipped with a 12.5 mm diameter disruptor horn. Transmission electron microscopy (TEM) and Field emission scanning electron microscopy (FESEM) images were recorded by FEI Tecnai G2 F20 S-Twin 200KV and Hitach S-4800 respectively. Fourier-transform infrared (FTIR) spectroscopy measurement was performed using a Thermo FTIR spectrometer. Raman spectra were measured on Horiba JY Labrain HR800 Raman spectroscopy (exciting source: 632 nm laser for Raman in air at room temperature). X-ray diffraction (XRD) patterns were obtained on X'Pert-Pro MPD (Cu-K α). N₂ adsorption/desorption analyses were carried out at 77 K using Micromeritics ASAP 2050. Electrochemical performance analyses (cyclic voltammeter (CV) curves, galvanostatic charge-discharge test and electrochemical impedance spectroscopy (EIS) measurements) were recorded by CHI660C electrochemical work station. EIS measurements were carried out at 0 V by imposing a sinusoidal perturbation of 10 mV over the frequency range from 0.01 Hz to 1 MHz.

RESULTS AND DISCUSSIONS

Morphology and Formation Mechanism



Scheme 1. Schematic illustration for the formation mechanism of wrinkled graphene layer.

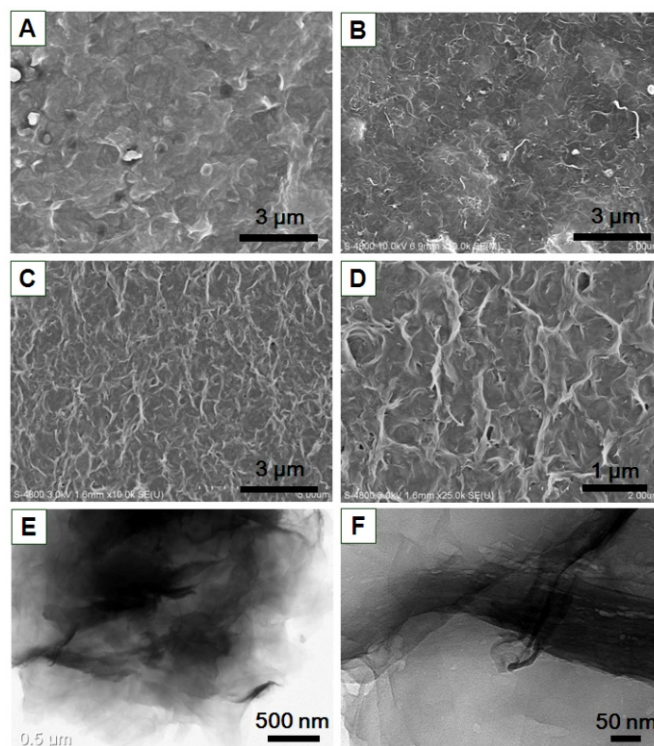


Figure 1. Top view SEM images of A) RGO/PANI/IL, B) RGO/PANI/MWCNT, C) RGO/PANI/MWCNT/IL (under low magnification) and D) RGO/PANI/MWCNT/IL (under high magnification). TEM images of RGO/PANI/MWCNT/IL: E) under low magnification and F) under high magnification.

The top view SEM images of RGO/PANI/IL, RGO/PANI/MWCNT and RGO/PANI/MWCNT/IL are shown in Figure 1A-D. As shown in Figure 1C and 1D, the RGO/PANI/MWCNT/IL exhibited an interesting surface morphology, in which the surface was full of wrinkles and pores formed by the over-contraction of RGO/PANI layers. The structure details of these wrinkles could also be found in their TEM images as shown in Figure 1E (low magnification) and 1F (high magnification). From the TEM images, it could be observed that the wrinkled RGO/PANI layers exhibited a fluffy and porous structure since the wrinkles hindered their over-stacking. Moreover, very few MWCNTs could be observed in their TEM images. In order to understand the formation mechanism of the wrinkled structure of RGO/PANI/MWCNT/IL composites, we compared its morphology with those of RGO/PANI/IL and RGO/PANI/MWCNT respectively. Very different from RGO/PANI/MWCNT/IL composite film, RGO/PANI/IL and RGO/PANI/MWCNT composite films both exhibited smooth surfaces and the carbon nanotubes could be clearly observed in RGO/PANI/MWCNT composite film. Considering the morphology differences between RGO/PANI/MWCNT/IL and the other two composite films, a suggested formation mechanism for the wrinkled structure of RGO/PANI/MWCNT/IL composite film was proposed (Scheme 1). Since both the carbon nanotubes and EMIBF₄ are

necessary for the formation of the wrinkled structure, there are at least three kinds of interactions existing in the system: the π - π^* interaction between RGO/PANI and MWCNT,³³ the π - π^+ interaction between MWCNT and EMI^+ ,³⁴ and the electrostatic force between EMI^+ and BF_4^- . During the formation process of RGO/PANI/MWCNT/IL composite film, since the components were bound together through the above two interactions, when EMI^+ and BF_4^- ions began to get close to each other caused by the electrostatic interactions, the MWCNTs which anchored on the RGO/PANI layer also moved together and its movement caused the squeezing of the RGO/PANI layer. As a result, the wrinkles were formed which resulted in larger surface area of the composite film. Moreover, the MWCNTs were usually wrapped in the RGO/PANI wrinkles. That's also why MWCNTs could hardly be observed in RGO/PANI/MWCNT/IL composite film. Along with the formation of these wrinkles, due to the contraction of the RGO/PANI layers, pores also generated at the connection sites where the RGO/PANI layers should have overlapped together. As the RGO/PANI/MWCNT/IL film was used as the electrode film for supercapacitors, these pores provided more ways to let the electrolyte ions quickly immigrate into the electrode layer and thus increased the charge-discharge capacitance and other electrochemical performances.

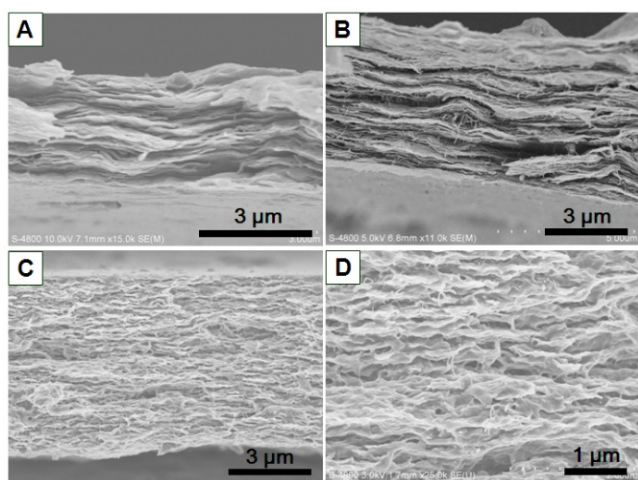


Figure 2. SEM images of A) RGO/PANI/IL, B) RGO/PANI/MWCNT, C) RGO/PANI/MWCNT/IL (under low magnification) and D) RGO/PANI/MWCNT/IL (under high magnification) from side view.

Not only increasing the surface area and pores at the interface, but also the wrinkles made the whole electrode film exhibiting a 3D porous structure which could offer a great larger surface area than 2D RGO/PANI films. From the side view SEM images of RGO/PANI/IL, RGO/PANI/MWCNT and RGO/PANI/MWCNT/IL films shown in Figure 2, it could be clearly observed that very different from the closely stacked RGO/PANI layers in RGO/PANI/IL and RGO/PANI/MWCNT composite films, the whole RGO/PANI/MWCNT/IL electrode film exhibited a fluffy structure since the wrinkles separated the neighboring RGO/PANI layers. The enlargement of the space

between neighboring RGO/PANI layers also led to the variation in the thickness of the composite films. The thickness was about 3 μm for RGO/PANI/IL film and 4 μm for RGO/PANI/MWCNT film. For RGO/PANI/MWCNT/IL composite film, its thickness was high up to 6.7 μm which was caused by the wrinkles. Moreover, as mentioned above, fewer MWCNTs could be observed in the composite film as they were wrapped in the wrinkles, except for some very long carbon nanotubes extruded from the RGO/PANI layers.

Structural Characterization

The composition of the obtained products was characterized by FTIR and Raman spectra. In the FTIR spectra as shown in Figure 3A, RGO displayed obvious peaks at 3436 and 2919 cm^{-1} , which corresponded to $-\text{O}-\text{H}$, $-\text{C}-\text{H}$ stretching vibrations, respectively.²³ These results were attributed to the presence of partially reduced graphene oxide sheets. Compared with the FTIR spectrum of RGO, the characteristic peaks of PANI could be observed in the spectra of RGO/PANI, RGO/PANI/MWCNT and RGO/PANI/MWCNT/IL composite films. The peaks at 1562, 1481, 1388 and 806 cm^{-1} were attributed to the vibrations of $-\text{C}=\text{N}$, $-\text{C}=\text{C}$, $-\text{C}-\text{N}$, and $-\text{C}-\text{H}$ respectively, which demonstrated the existence of PANI in the composite films.²³ Moreover the specific peak of EMIBF_4 at 1037 cm^{-1} , which corresponded to the $-\text{B}-\text{F}$ vibration³⁵, could be observed in the spectrum of RGO/PANI/MWCNT/IL composite film.

The graphitization degree of carbon nanomaterials could be characterized by Raman spectrum. From the Raman spectra of the obtained products as shown in Figure 3B, the RGO displayed the well-documented D band at 1327 cm^{-1} and G band at 1586 cm^{-1} , corresponding to the disordered graphitic carbon and the E_{2g} vibration of the sp^2 bonded carbon atoms, respectively.³⁶ The characteristic Raman peaks of PANI at 1157, 1404 and 1504 cm^{-1} could be observed in the Raman spectra of the three PANI contained composite films, which were attributed to C-H bending of the quinoid ring, electronic absorption of free charge carriers and N-H bending.³⁷ Moreover, the peaks at 606, 1404 and 1504 cm^{-1} , which correspond to the cross-linked portion of PANI, were very weak, indicating that the RGO may alleviate the PANI reticulation. After the addition of EMIBF_4 , its characteristic peaks at 746, 1457 and 1563 cm^{-1} appeared, which was attributed to the intramolecular vibrations of the nonplanar EMI^+ .³⁸ There were two interesting phenomena existing in the Raman spectrum of RGO/PANI/MWCNT/IL composite film. Compared with RGO/PANI/MWCNT film, after the addition of IL, the characteristic peaks of PANI were obviously enhanced. This was due to the fluorescence of small IL molecules which enhanced the stimulated Raman scattering of PANI.³⁹ On the other hand, after the addition of IL, the D band and G band peak positions of RGO and MWCNT were shifted from 1327 and 1586 cm^{-1} to 1336 and 1599 cm^{-1} respectively. This could be ascribed to the generated strain in the composite film which was caused by the contraction of RGO/PANI layers.⁴⁰

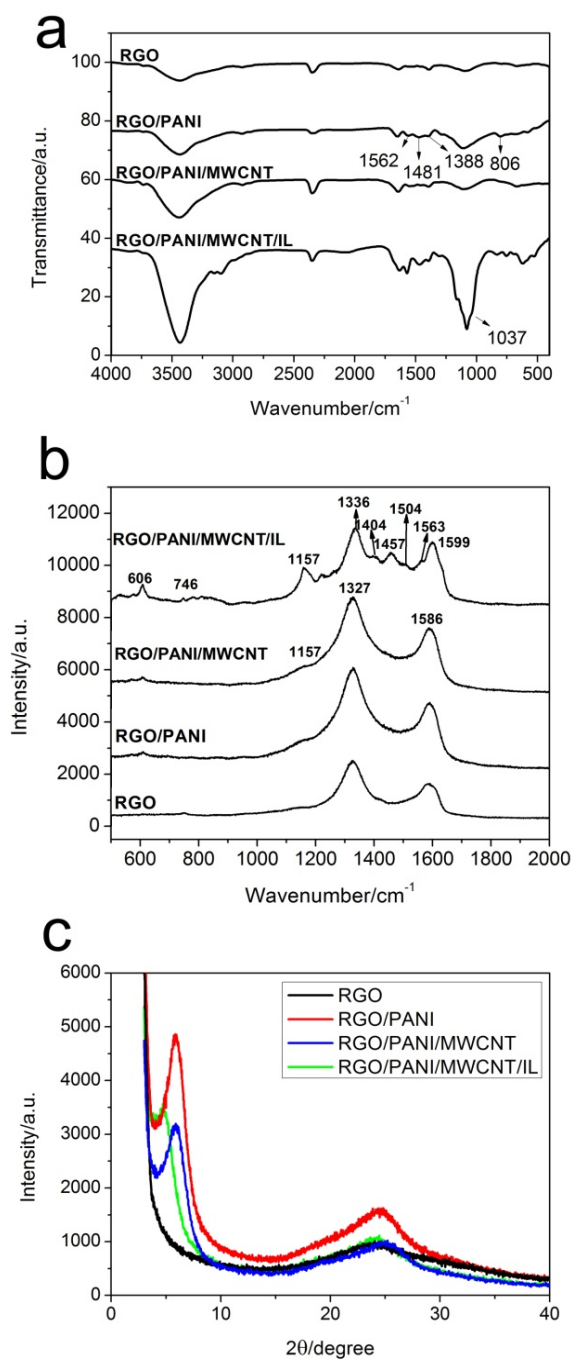


Figure 3. a) FTIR, b) Raman and c) XRD spectra for RGO, RGO/PANI, RGO/PANI/MWCNT and RGO/PANI/MWCNT/IL composite films.

In the structure of the obtained RGO/PANI based composite films, not only mesopores, but also micropores existed as the interlayer space between neighboring restacked RGO/PANI layers. Even when the RGO/PANI layers were separated by wrinkles, few-stacked-layers also existed. XRD spectra were used to characterize the micropore structure as well as the interlayer spacing of the composite films.⁴¹ As shown in Figure 3C, the characteristic peak at $2\theta=24.50^\circ$ corresponded to a

typical interlayer spacing of 0.363 nm for restacked RGO layers.²³ After the RGO sheet was coated by a thin PANI layer, its π - π interaction as well as the degree of over-stacking was alleviated, and thus the interlayer spacing was enlarged to 1.47 nm ($2\theta=5.85^\circ$). The intercalation of MWCNT into the RGO/PANI layers cause no variation to the interlayer spacing between few-stacked-layers, since the enlarged interlayer spacing caused by the intercalation of MWCNT was too large to be detected by XRD spectra. The interlayer spacing was then expanded to 1.87 nm ($2\theta=4.72^\circ$) for RGO/PANI/MWCNT/IL composite since IL could diffuse into the RGO/PANI layers.⁴¹ Considering the calculated diameter of symmetric BF_4^- anion was 0.47 nm and the lateral dimension of slightly oblong shaped EMI^+ cation was 0.54-0.95 nm⁴², the enlarged interlayer spacing of RGO/PANI/MWCNT/IL was more fit for ion insertion since it could accommodate more electrolyte ions.

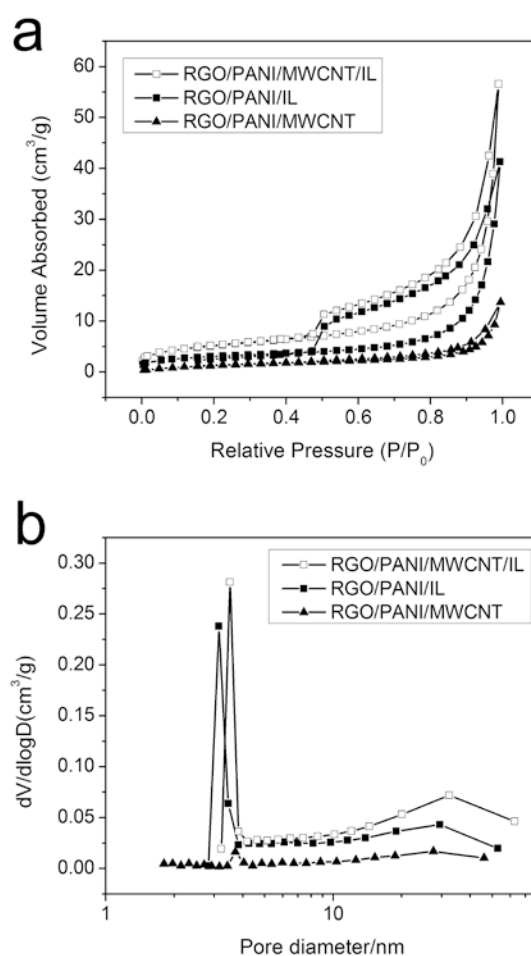


Figure 4. a) Nitrogen adsorption-desorption isotherm and b) pore-size distribution of rinsed RGO/PANI/IL, RGO/PANI/MWCNT, and RGO/PANI/MWCNT/IL films.

As IL contained in the composite film may cover the surface of other components, the accurate surface area and pore diameter distribution of the composite films could only be obtained after the IL was washed out with water. The analyzed

results were shown in Figure 4. According to BDDT classification, the three samples all exhibited type IV isotherms with H4 hysteresis loop at a relative high pressure which were due to the incomplete desorption of N_2 from narrow slit-like pores.⁴³ The calculated BET surface area of the rinsed RGO/PANI/MWCNT/IL was $18.11 \text{ m}^2/\text{g}$, while those of the rinsed RGO/PANI/IL and RGO/PANI/MWCNT were $10.57 \text{ m}^2/\text{g}$ and $5.21 \text{ m}^2/\text{g}$ respectively. From the pore size distribution curves as shown in Figure 4b, a more direct result about the pore structure of the three samples could be observed. All of the three samples exhibited two peaks centered at 2-4 nm and in the range of 10-60 nm, which corresponded to the small and large mesopores respectively. The small mesopores originated from the carbon materials themselves, including the inner cavity of carbon nanotubes and the interspaces between closely restacked graphene layers. The large mesopores corresponded to the enlarged interspace caused by the MWCNTs insertion and graphene wrinkles. Among them, both RGO/PANI/MWCNT and RGO/PANI/IL exhibited low peaks in the range of 20-50 nm, indicating fewer large mesopores existed in their structure. However, for RGO/PANI/MWCNT/IL composite film, the intensity of the peak in the range of 10-60 nm was obviously enhanced and the peak position was also removed toward high value, which indicated more pores with larger size appeared in its structure. The analyzed result was also in good agreement with the SEM observation results as shown in Figure 2.

Electrochemical Properties

For flexible supercapacitors, IL was always used as the electrolyte since it could work at higher voltage and exhibit high safety, high environmental and thermal stability. However, limited by the slow immigration rate of the IL ions, among the reported results, few IL electrolyte based all-solid-state supercapacitors could exhibit capacitances higher than 150 F/g .⁴⁴⁻⁴⁷ In our experiment, the supercapacitor performances of RGO/PANI/IL, RGO/PANI/MWCNT and RGO/PANI/MWCNT/IL electrode films were evaluated by means of CV, galvanostatic charge-discharge and cycling-life tests in two-electrode systems. As shown in Figure 5a, the CVs of the composite electrode films exhibited nearly rectangular shape in the potential window of 0~1.5 V, demonstrating their electrical double layer capacitive properties. Among them, the CV curve of RGO/PANI/MWCNT/IL electrode film exhibited larger enclosed area than the other two, indicating its better capacitive performance. Specific capacitances of the three composite electrode films were calculated according to the galvanostatic charge-discharge curves (Figure 5b-d) and the calculated results at different charge-discharge current densities were given in Figure 5e. The galvanostatic charge-discharge tests were also performed in a potential range from 0 to 1.5 V. The almost symmetrical charge and discharge curves demonstrated their good and stable capacitive behavior in the wide potential window. As shown in Figure 5b-d, under different current densities, RGO/PANI/MWCNT/IL exhibited

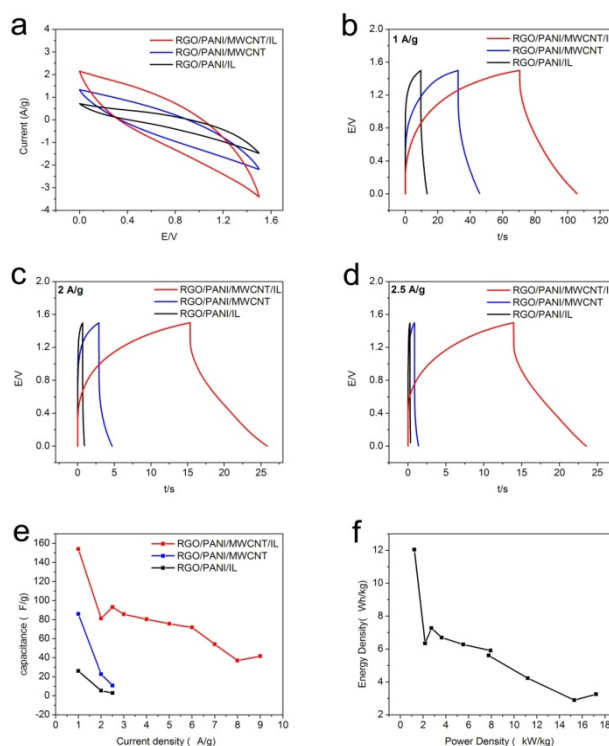
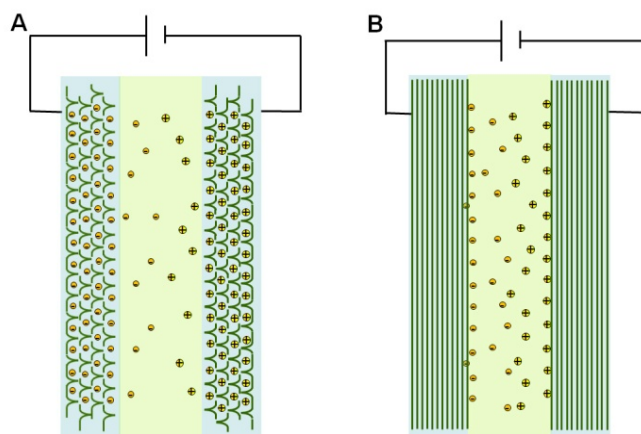


Figure 5. Electrochemical performance of the supercapacitors based on RGO/PANI/IL, RGO/PANI/MWCNT, and RGO/PANI/MWCNT/IL electrode films. a) CV curves at scan rate of 0.1 V s^{-1} in the potential range from 0 to 1.5 V; b-d) Galvanostatic charge-discharge curves at different current densities; e) Specific capacitance at different current densities; f) Ragone plot of supercapacitors based on RGO/PANI/MWCNT/IL electrode films.



Scheme 2. Comparison of different ion storage behaviors between porous and closely restacked RGO/PANI composite electrode based supercapacitors.

higher charge-discharge time as well as capacitance than the other two electrode membranes. At a current density of 1 A/g , the RGO/PANI/MWCNT/IL electrode film exhibited a high capacitance of 154.12 F/g , while the capacitances of RGO/PANI/IL and RGO/PANI/MWCNT were 26.07 and 85.86

F/g respectively. Their different capacitances were mainly determined by the different interlayer spacing and porosity of the three composite films. In RGO/PANI/MWCNT/IL composite film, the wrinkled RGO/PANI film exhibited a fluffy and porous structure since the wrinkles hindered the over-stacking of the RGO/PANI layers and thus increased the interlayer spacing. Since larger interlayer spacing could accommodate more electrolyte ions, its capacitance was comparatively high. (Scheme 2) When the current density increased, the specific capacitance usually decreased since the decreased charge-discharge time was not enough for the immigration of all the electrolyte ions into the electrode layer. Under this circumstance, fast immigration process of electrolyte ions was helpful for keeping high capacitance at high current densities. From Figure 5e, it could be found that the capacitance retention of RGO/PANI/MWCNT/IL was exceptionally higher than the other two electrode films. At the current density of 2.5 A/g, the specific capacitance was 93.09 F/g, higher than a half of its capacitance at low current density of 1 A/g, while the values for RGO/PANI/IL and RGO/PANI/MWCNT were only 2.91 and 10.85 F/g, only approximately 1/9 and 1/8 of their capacitances at low current density. Moreover, the specific capacitances of RGO/PANI/IL and RGO/PANI/MWCNT at current densities higher than 2.5 A/g were not able to be measured since they were too low. However, the specific capacitance of RGO/PANI/MWCNT/IL still remained higher than 40 F/g at current density of 9 A/g. The higher capacitance retention ability of RGO/PANI/MWCNT/IL electrode film at high current density could be ascribed to its 3D wrinkled structure which offered more space for the transportation of the electrolyte ions. As a result, even at high current densities, the electrolyte ions could still quickly immigrated to the electrode layer and thus the capacitance was well kept. Moreover, the capacitance value of RGO/PANI/MWCNT/IL at a current density of 2.5 A/g was slightly higher than that measured at 2A/g. This was due to the constant effect of ion insertion into the electrode layer during the charge-discharge test. Since the two current densities were very close, when more ions existed in the electrode layer, the capacitance did not fall but slightly arose at the current density of 2.5 A/g. This phenomenon was also reported by other groups.^{23, 48}

Ragone plots of the RGO/PANI/MWCNT/IL electrode film based supercapacitor were shown in Figure 5f. Along with the increase of the charge-discharge current density, the energy density decreased and the power density increased. Owing to the facile ion transportation process and the wide electrochemical potential window of the system, the flexible supercapacitor exhibited both high energy density and power density which were 12.04 Wh/kg and 1.23 kW/kg at 1 A/g; and 3.25 Wh/kg and 17.21 kW/kg at 9 A/g. The obtained values of the RGO/PANI/MWCNT/IL based supercapacitor were higher than the values of other RGO/PANI based supercapacitors reported elsewhere¹⁹⁻²⁰.

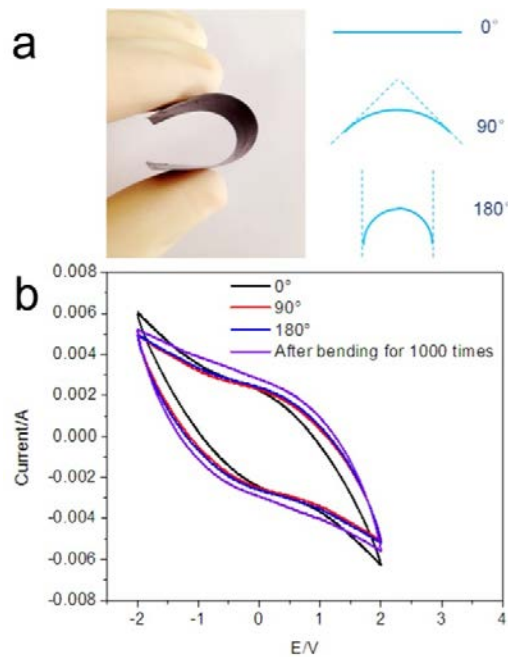


Figure 6. a) Images and schematics of a flexible film supercapacitor in different bending states; b) CV curves of the film supercapacitor at scan rates of 1 V s^{-1} when bent by 0° , 90° , 180° and after being bent for 1000 times.

To test the flexibility of the film and the influence of its flexibility on electrochemical performances, the picture and schematics of the bended supercapacitor strip was shown in Figure 6a and the CV curves of the strip under different bending state and after bending for 1000 times were shown in Figure 6b. The results proved the perfect flexibility of the supercapacitor. When the film capacitor was bent to 90° and 180° , its capacitance was not dropped according to their CV curves. Moreover, after manually bending it for 1000 times, the capacitance was even slightly increased, and this may be due to the ion insertion into the electrode layer which was caused by the bending process of the capacitor strip.⁴⁹

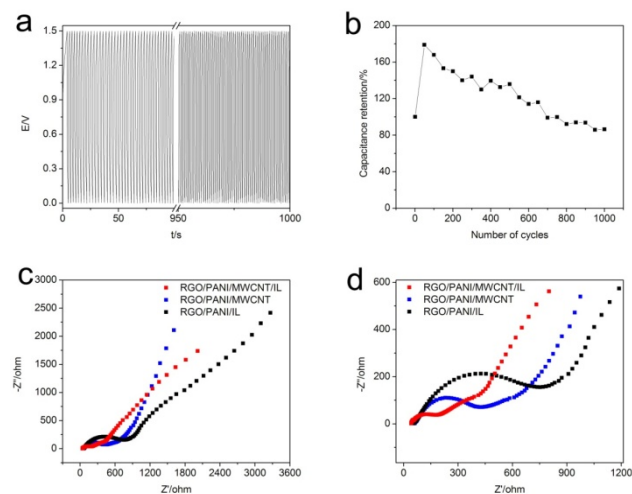


Figure 7. a,b) capacitance retention over 1000 cycles at 10 A g^{-1} ; c,d) Nyquist plots of supercapacitors based on RGO/PANI/IL, RGO/PANI/MWCNT, and RGO/PANI/MWCNT/IL electrode films.

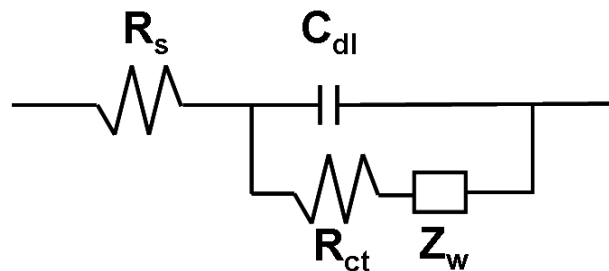


Figure 8. Equivalent circuit model for the RGO/PANI based nanocomposite electrochemical system.

The endurance galvanostatic charge-discharge experiment was also carried out to study the cyclic stability of the composite materials. As shown in Figure 7a and 7b, the capacitance of RGO/PANI/MWCNT/IL first increased to about 179% to its original capacitance after 50 cycles. This was because more electrolyte ions diffused into the electrode layer to reach equilibrium in the first 50 cycles. As a result, the capacitance increased. Then, along with cyclic charge-discharge process, the specific capacitance gradually decreased during the following 950 cycles. However, after 1000 cycles, its capacitance was still maintained higher than 85% of its original value. EIS spectroscopy is a powerful tool to study the electrochemical behavior of the electrode membranes. From the Nyquist plots as shown in Figure 7c and 7d, the observed semicircle in the left portion corresponds to a higher-frequency region, whereas the inclined portion corresponds to the low-frequency. The depression in the semicircle is modeled as the parallel combination of an interfacial charge transfer resistance (R_{ct}) and double-layer capacitance (C_{dl}) and the inclined portion at low-frequency represents the ion diffusion in the electrode pores⁵⁰. Based on the above analysis, the equivalent circuit model for our system contains the bulk resistance R_s , the contact capacitance C_{dl} which is parallel with contact resistance R_{ct} and a Warburg diffusion element attributed to the diffusion of ions (Z_w) (Figure 8). The bulk resistance (R_s) was the sum of the electrolyte resistance, electrode resistance and the contact resistance at the electrode-electrolyte layer.³⁴ Based on the fitted results of the equivalent circuit model, the calculated R_s of RGO/PANI/MWCNT/IL based capacitor was only 57.5Ω , less than the other two capacitors based on RGO/PANI/MWCNT and RGO/PANI/IL electrode films, which were 79.34Ω and 76.09Ω respectively. Moreover, compared to RGO/PANI/IL and RGO/PANI/MWCNT composite electrodes, the EIS spectrum of RGO/PANI/MWCNT/IL at high frequency exhibited the semicircle with relatively smaller radius, which corresponded to a smaller charge transfer resistance caused by the Faradic reactions and the double-layer capacitance on the grain surface.

The calculated R_{ct} was 97.03Ω for RGO/PANI/MWCNT/IL based capacitor, and were 235Ω and 127.1Ω for the other two capacitors based on RGO/PANI/MWCNT and RGO/PANI/IL electrode films respectively.

Conclusions

In summary, a typical kind of 3D RGO/PANI based electrode film was prepared by using MWCNT and IL as the surfactant-like agent in the assembly process. By using this method, the pore structure of the obtained 3D electrode film could be well controlled as micro and mesopores, which afforded them high electrochemical performances as electrode membranes for supercapacitors. Electrochemical studies demonstrated their high specific capacitance of 154.12 F/g , as well as high energy density and power density, which were 12.04 Wh/kg and 1.23 kW/kg at the current density of 1 A/g and 13.25 Wh/kg and 17.21 kW/kg at the current density of 9 A/g . The supercapacitor also showed excellent stability, as its specific capacitance still maintained higher than 85% of its original value after 1000 charge-discharge cycles. The as-prepared all-solid-state supercapacitor may hold great promise for low-cost and high-performance flexible energy storage applications.

Acknowledgements

We thank the Natural Science Foundation for Distinguished Young Scientists of Jiangsu Province (BK2012008), the Hong Kong, Macao and Taiwan Science & Technology Cooperation Program of China (2012DFH50120), the National Natural Science Foundation of China (21373263, 11204350, 51303204), the China Postdoctoral Science Foundation (2013M531416), the External Cooperation Program of BIC, Chinese Academy of Science (121E32KYSB20130009) and the National Basic Research Program of China (2010CB934700).

Notes and references

i-Lab, Suzhou Institute of Nano-Tech and Nano-Bionics, Chinese Academy of Sciences, Suzhou, 215123 (P. R. China). E-mail: wchen2006@sinano.ac.cn

- 1 L. Nyholm, G. Nyström and A. Mihranyan, *Adv. Mater.*, 2011, **23**, 3751–3769.
- 2 H. Gwon, H. S. Kim, K. U. Lee, D. H. Seo, Y. C. Park, Y. S. Lee, B. T. Ahn and K. Kang, *Energy Environ. Sci.*, 2011, **4**, 1277–1283.
- 3 F. Liu, S. Y. Song, D. F. Xue and H. J. Zhang, *Adv. Mater.*, 2012, **24**, 1089–1094.
- 4 P. Simon and Y. Gogotsi, *Nat. Mater.*, 2008, **7**, 845–854.
- 5 G. Wang, L. Zhang and J. Zhang, *Chem. Soc. Rev.*, 2012, **41**, 797–828.
- 6 P. J. Hall, M. Mirzaei, S. I. Fletcher, F. B. Sillars, A. J. R. Rennie, G. O. Shitta-Bey, G. Wilson, A. Cruden and R. Carter, *Energy Environ. Sci.*, 2010, **3**, 1238–1251.
- 7 Y. J. Kang, S. J. Chun, S. S. Lee, B. Y. Kim, J. H. Kim, H. Chung, S. Y. Lee and W. Kim, *ACS Nano*, 2012, **6**, 6400–6406.
- 8 S. A. Sherrill, P. Banerjee, G. W. Rubloff and S. B. Lee, *Phys. Chem. Chem. Phys.* 2011, **13**, 20714–20723.

- 9 Y. Jin, H. Y. Chen, M. H. Chen, N. Liu and Q. W. Li, *ACS Appl. Mater. Interfaces*, 2013, **5**, 3408–3416.
- 10 H. C. Gao, F. Xiao, C. B. Ching and H. W. Duan, *ACS Appl. Mater. Interfaces*, 2012, **4**, 7020–7026.
- 11 V. Gupta and N. Miura, *Electrochim. Acta*, 2006, **52**, 1721–1726.
- 12 H. Zhang, G. P. Cao, W. K. Wang, K. G. Yuan, B. Xu, W. F. Zhang, J. Cheng and Y. S. Yang, *Electrochim. Acta*, 2009, **54**, 1153–1159.
- 13 J. Huang and R. B. Kaner, *Chem. Commun.*, 2006, **4**, 367–376.
- 14 L. Z. Fan, Y. S. Hu, J. Maier, P. B. Adelhelm and M. Smarsly, *Adv. Funct. Mater.*, 2007, **17**, 3083–3087.
- 15 Z. Gao, W. L. Yang, J. Wang, H. J. Yan, Y. Yao, J. Ma, B. Wang, M. L. Zhang and L. H. Liu, *Electrochim. Acta*, 2013, **91**, 185–194.
- 16 T. Sugino, K. Kiyohara, I. Takeuchi, K. Mukai and K. Asaka, *Carbon*, 2011, **49**, 3560–3570.
- 17 H. Zengin, W. Zhou, J. Jin, R. Czerw, Jr. D. W. Smith and L. Echegoyen, *Adv. Mater.*, 2002, **14**, 1480–1483.
- 18 M. Cochet, W. K. Maser, A. M. Benito, M. A. Callejas, M. T. Martínez, J. M. Benoit, J. Schreiberb and O. Chauvet, *Chem. Commun.*, 2001, 1450–1451.
- 19 Q. Wang, J. Yan, Z. J. Fan, T. Wei, M. L. Zhang and X. Y. Jing, *J. Power Sources*, 2014, **247**, 197–203.
- 20 L. Li, A. O. Raji, H. L. Fei, Y. Yang, E. L. G. Samuel and J. M. Tour, *ACS Appl. Mater. Interfaces*, 2013, **5**, 6622–6627.
- 21 Q. Liu, O. Nayfeh, M. H. Nayfeh and S. H. Yau, *Nano Energy*, 2013, **2**, 133–137.
- 22 M. Sawan gphruk, M. Suksomboon, K. Kongsupornsak, J. Khuntilo, P. Srimuk, Y. Sanguansak, P. Klunbud, P. Suktha and P. Chiochan, *J. Mater. Chem. A*, 2013, **1**, 9630–9636.
- 23 Y. Meng, K. Wang, Y. J. Zhang and Z. X. Wei, *Adv. Mater.*, 2013, **48**, 6985–6990.
- 24 C. Li and G. Shi, *Nanoscale*, 2012, **4**, 5549–5563.
- 25 E. Frackowiak and F. Béguin, *Carbon*, 2001, **39**, 937–950.
- 26 K. Jurewicz, C. Vix-Guterl, E. Frackowiak, S. Saadallah, M. Reda, J. Parmentier, J. Patarin and F. Béguin, *J. Phys. Chem. Solids*, 2004, **65**, 287–293.
- 27 S. R. Guo, W. Wang, C. S. Ozkan and M. Ozkan, *Journal of Materials Research*, **28**, 918–926.
- 28 P. Bharmoria, T. Singh and A. Kumar, *J. Colloid Interface Sci.*, 2013, **407**, 361–369.
- 29 D. Li, M. B. Muller, S. Gilje, R. B. Kaner and G. G. Wallace, *Nat. Nanotechnol.*, 2008, **3**, 101–105.
- 30 M. D. Stoller and R. S. Ruoff, *Energy Environ. Sci.*, 2010, **3**, 1294–1301.
- 31 T. Brousse, M. Toupin and D. Belanger, *J. Electrochem. Soc.*, 2004, **151**, A614–A622.
- 32 H. C. Gao, F. Xiao, C. B. Ching and H. W. Duan, *ACS Appl. Mater. Interfaces*, 2012, **4**, 2801–2810.
- 33 T. Yang, Q. Guan, L. Meng, R. R. Yang, Q. H. Li and K. Jiao, *RSC Adv.*, 2013, **3**, 22430–22435.
- 34 T. Fukushima, A. Kosaka, Y. Ishimura, T. Yamamoto, T. Takigawa, N. Ishii and T. Aida, *Science*, 2003, **300**, 2072–2074.
- 35 T. Zheng, S. T. Ren, Q. Zhou, Q. Li, L. Y. Zhang, H. Y. Li and Y. Lin, *J. Polym. Res.*, 2014, **21**, 361.
- 36 H. P. Cong, Ren, X. C.; Wang, P.; Yu, S. H. *Energy Environ. Sci.*, **2013**, **6**, 1185–1191.
- 37 L. R. Kong, X. F. Lu and W. J. Zhang, *J. Solid State Chem.*, 2008, **181**, 628–636.
- 38 Y. Umebayashi, T. Fujimori, T. Sukizaki, M. Asada, K. Fujii, R. Kanzaki and S. Ishiguro, *J. Phys. Chem. A*, 2005, **109**, 8976–8982.
- 39 X. Q. Zhong, X. B. Cheng, L. H. Jin, J. G. Yang, *Chinese Journal of Light Scattering*, 2000, **11**, 293–296.
- 40 W. Yang, R. Z. Wang, H. Yan, *Phys. Rev. B*, 2008, **77**, 195440.
- 41 X. W. Yang, C. Cheng, Y. F. Wang, L. Qiu and D. Li, *Science*, 2013, **341**, 534–537.
- 42 I. Must, F. Kaasik, I. Pöldsalu, U. Johanson, A. Punning and A. Aabloo, *Carbon*, 2012, **50**, 535–541.
- 43 K. S. W. Sing, D. H. Everett, R. A. W. Haul, L. Moscou, R. A. Pierotti, J. Rouquerol and T. Siemieniewska, *Pure Appl. Chem.*, 1985, **57**, 603–619.
- 44 Sellam and S. A. Hashmi, *ACS Appl. Mater. Interfaces*, 2013, **5**, 3875–3883.
- 45 Sellam and S. A. Hashmi, *J. Solid State Electrochem.*, 2014, **18**, 465–475.
- 46 J. Torop, V. Palmre, M. Arulepp, T. Sugino, K. Asaka and A. Aabloo, *Carbon*, 2011, **49**, 3113–3119.
- 47 J. S. Bonso, G. D. Kalawa and J. P. Ferraris, *J. Mater. Chem. A*, 2014, **2**, 418–424.
- 48 H. L. Wang, Q. M. Gao and J. Hu, *J. Power Sources*, 2010, **195**, 3017–3024.
- 49 R. Tiwari and E. Garcia, *Smart Mater. Struct.* 2011, **20**, 083001.
- 50 Y. J. Kang, H. Chung, C. H. Han and W. Kim, *Nanotechnology*, 2012, **23**, 065401.